





A force/position controller free of velocity measurement for robot manipulators with bounded torque input

César A. CHÁVEZ-OLIVARES , Marco O. MENDOZA-GUTIÉRREZ ,
Isela BONILLA-GUTIÉRREZ  and Emilio J. GONZÁLEZ-GALVÁN 

Robot manipulators play a crucial role in various industrial and research settings, requiring precise and controlled interactions with their surroundings. Achieving this goal with fewer sensors offers advantages not only in terms of cost and decreased risk of failure but also enhances accuracy and long-term reliability. In this paper, we introduce a nonlinear force/position controller that eliminates the requirement for velocity measurements. This controller provides versatility by facilitating the generation of bounded control actions during robot-environment interactions, ensuring a higher level of safety for both the robot and its environment during the execution of tasks necessitating physical contact between them. The proposed approach is underpinned by a stability analysis in the Lyapunov sense and has been validated through a series of simulation and experimental tests.

Key words: force/position control, Lyapunov stability, robot manipulator, saturation function

1. Introduction

Robot manipulators play a vital role in numerous industrial and research applications, where precise and delicate interactions with the environment are necessary [1–3]. Over recent years, there has been a burgeoning interest in expanding the capacities of robots beyond conventional position control [4–6]. The

Copyright © 2024. The Author(s). This is an open-access article distributed under the terms of the Creative Commons Attribution-NonCommercial-NoDerivatives License (CC BY-NC-ND 4.0 <https://creativecommons.org/licenses/by-nc-nd/4.0/>), which permits use, distribution, and reproduction in any medium, provided that the article is properly cited, the use is non-commercial, and no modifications or adaptations are made

C.A. Chávez-Olivares is with Robotics Engineering Department, Autonomous University of Aguascalientes, Prol. Mahatma Gandhi 6601, Aguascalientes, 20340, Aguascalientes, Mexico.

M.O. Mendoza-Gutiérrez and I. Bonilla-Gutiérrez (corresponding author, e-mail: isela.bonilla@uaslp.mx) are with Faculty of Sciences, Autonomous University of San Luis Potosí, Av. Chapultepec 1570, Privadas del Pedregal, San Luis Potosí, 78295, San Luis Potosí, Mexico.

E.J. González-Galván is with Faculty of Engineering, Autonomous University of San Luis Potosí, Dr. Manuel Nava 8, Zona Universitaria Poniente, San Luis Potosí, 78290, San Luis Potosí, Mexico.

Received 6.03.2024.. Revised 19.05.2024.

development of force and impedance control techniques has unveiled novel opportunities to achieve interactions with the surrounding world that are not only safer and more efficient but also adaptive [7–9].

Force control embodies the capacity of a robot to regulate the forces it applies to or detects from its environment. Unlike traditional position control, which concentrates on achieving precise joint positions, force control empowers robots to execute tasks using a specific force, enabling them to handle delicate objects, conduct intricate assembly tasks, and even engage safely in human-robot collaboration [8, 10–12]. Conversely, impedance control is a complementary concept that delineates the robot's capability to adjust its behavior in response to external forces. By simulating compliance and elasticity, the robot can naturally react to alterations in its surroundings, thereby averting damage to itself, the environment, or any humans with whom it interacts. Impedance control proves especially valuable in applications such as physical human-robot interaction, where rigid and inflexible movements could potentially pose risks [9, 13, 14]. These two techniques encompass the primary categories used to classify various robot-environment interaction control algorithms. The first directly regulates force, while the second achieves this indirectly.

Given the substantial rise in automated tasks necessitating interaction between robots and their environment, interaction control stands as an advanced and crucial research area in robotics and automation. This technology seeks to empower robots to exert and manage interaction (contact) forces. It hinges on a fusion of sensor data, incorporating joint position/velocity sensors and force/torque sensors, to oversee force interactions with the environment [15, 16]. Owing to the multitude of approaches explored by various researchers, the solutions offered for resolving interaction control can be categorized into the following groups:

- *Adaptive control*: These strategies are commonly employed to adjust control parameters in real-time based on sensor feedback. This enhances the accuracy of force control, particularly in situations involving dynamic and uncertain environments [13, 17].
- *Machine learning*: These techniques, such as neural networks and reinforcement learning, are increasingly applied to enhance model-less force control. These algorithms can learn complex force-control policies from data, improving adaptability [18–20].
- *Impedance/admittance control*: These techniques are widely used for sensorless force control. They define the relationship between force and displacement, allowing robots to exhibit compliant behavior when interacting with objects and humans, or performing tasks like assembly [14, 21].

- *Force sensing in end-effector*: Some approaches integrate force sensors directly into the robot's end-effector, allowing for direct force measurements at the point of contact. These sensors are critical for accurate force control [22–24].
- *Vision-based force control*: Vision systems, such as cameras and depth sensors, are incorporated into sensorless force control algorithms. They provide visual feedback to estimate contact forces during tasks like grasping and manipulation [25, 26].
- *Tactile sensing*: Tactile sensors integrated into robot fingertips or end-effectors provide valuable information about contact forces and object properties. Combining tactile feedback with other sensorless control methods enhances performance [27–29].
- *Sensorless force control*: It often relies on dynamic models of the robot and its interactions with the environment. These models use sensor data, primarily joint positions, torque measurements, and currents of the motors, to estimate contact forces and control their application [30–34].

The control schemes that rely on velocity and acceleration sensors come with certain limitations and challenges. Firstly, the integration of such sensors adds to the overall complexity and cost of the robot system, making it less economically viable, particularly for smaller-scale applications or industries with budget constraints [35]. Additionally, the presence of sensors increases the likelihood of mechanical failures and requires regular maintenance, leading to potential downtime and increased operational costs. Moreover, the sensors can be susceptible to noise, drift, and calibration issues, which can degrade the accuracy and reliability of the control system over time [36]. In dynamic environments or during high-speed movements, the delay in sensor data acquisition and processing can lead to suboptimal control performance, potentially compromising the safety and efficiency of the robot. These limitations highlight the importance of exploring alternative control techniques based on a minimum number of sensors that can mitigate these issues and provide more robust and cost-effective solutions for robot manipulators [7].

In this work we are interested in the precise and direct control of force and motion of robot manipulators, without using velocity sensors. The issue of hybrid force/motion control over unknown rigid surfaces, where only position measurements are considered, is addressed in [37]. Their proposed solution relies on an extended state high-gain observer to concurrently estimate contact force and joint velocities. The authors provide both numerical simulations and experimental results. It is noteworthy that the experimental results exhibit slightly lower performance accuracy compared to the simulation results, indicating that this

discrepancy arises from uncertainties in the model and the presence of unknown external disturbances. In [38], the authors propose an integral sliding-mode observer for estimating external disturbances and velocity. They also introduce an application of a sensorless admittance controller scheme based on this observer. Their experimental results demonstrate high precision, bandwidth, and robustness. On the other hand, in [39], a sliding perturbation observer is developed for estimating assembly force without the reliance on a force sensor, and the need for velocity sensing is circumvented through the use of a sliding velocity estimator. This estimator is implemented on a dual-arm robot system, where actuators are controlled using drivers that estimate the rated torque by monitoring motor currents. The study verifies that the perturbation observer closely matches the actual torque provided by the drivers. However, it falls short in accurately representing the force estimation required for practical dual-arm assembly tasks.

The works mentioned above are intended for implementation in low-cost robotic platforms with only position sensors. However, these schemes have several significant drawbacks as follows:

- The response time of observers is slower compared to the real-time response of sensors.
- Observers exhibit noise in situations where there is no contact between the robot and the environment, which can cause instability.
- Most observers have a high degree of dependency on the accuracy of the model, and this is reflected in a decrease in the precision of the regulation of forces and/or movement.
- The cited works do not take into account limits on nominal torques imposed by the actuator drivers. Consequently, the schemes are not designed to accommodate input saturation on control torques, and this scenario is not considered in their stability analysis.
- The estimation techniques are employed exclusively for practical purposes within direct force control schemes, lacking a formal demonstration of stability [33]. Therefore, these observers are usually used only in indirect force regulation schemes as impedance/admittance controllers.

In order to study stability and generate bounded control actions, a nonlinear force/position controller is proposed in this study, which does not necessitate velocity measurements. The proposed approach directly regulates force and utilizes a linear filter for velocity estimation, thereby enhancing response speed compared to model-based observers. Furthermore, this controller offers versatility as it can be adapted to generate bounded control actions in robot-environment interaction tasks. The proposed scheme is underpinned by a stability analysis in the Lyapunov sense and is validated through a series of simulation and experimental tests.

2. Preliminaries

Let $A \in \mathbb{R}^{n \times m}$ with A_i and A_{ij} being the i -th row vector and (i, j) -th element of matrix A , respectively; and $y \in \mathbb{R}^n$ with y_i representing the i -th component of y ; while 0_n and I_n denote the origin of \mathbb{R}^n and the $n \times n$ identity matrix, respectively. In addition, $\|y\| = \sqrt{y^T y}$ is the Euclidean vector norm and $\|A\| = \sqrt{\lambda_{\max}\{A^T A\}}$ represents the induced matrix norm, with $\lambda_{\max}\{\cdot\}$ being the maximum eigenvalue.

Let $\zeta: \mathbb{R} \mapsto \mathbb{R}$ be a continuously differentiable scalar function and $\varphi: \mathbb{R} \mapsto \mathbb{R}$ be a locally Lipschitz, continuous, scalar function, both vanishing at zero, i.e., $\zeta(0) = \varphi(0) = 0$. Furthermore, ζ' denotes the derivative of ζ with respect to its argument, i.e., $\zeta'(\varsigma) = \partial\zeta(\varsigma)/\partial\varsigma$. While $D^+\varphi(\varsigma) = \limsup_{h \rightarrow 0^+} [\varphi(\varsigma + h) - \varphi(\varsigma)]/h$, $\forall \varsigma \in \mathbb{R}$, is the upper right-hand derivative, then $\varphi(\varsigma) = \int_0^\varsigma D^+\varphi(r) dr$ [40].

Definition 1. A nondecreasing Lipschitz-continuous function $\sigma: \mathbb{R} \rightarrow \mathbb{R}$ bounded by $M > 0$ is a generalized saturation function (GSF) if

(a) $\varsigma\sigma(\varsigma) > 0, \forall \varsigma \neq 0$.

(b) $|\sigma(\varsigma)| \leq M, \forall \varsigma \in \mathbb{R}$.

(c) In addition, if $\sigma(\varsigma) = \varsigma$ when $|\varsigma| \leq L$, for some $0 < L \leq M$, then σ is a linear generalized saturation function (L -GSF) for (L, M) .

Moreover, there is a constant $k > 0$ such that any generalized saturation function satisfies the following properties [11, 12]:

1. $\lim_{|\varsigma| \rightarrow \infty} D^+\sigma(\varsigma) = 0$.

2. $\exists \sigma'_M \in (0, \infty): 0 \leq D^+\sigma(\varsigma) \leq \sigma'_M, \forall \varsigma \in \mathbb{R}$.

3. $\frac{\sigma^2(k\varsigma)}{2k\sigma'_M} \leq \int_0^\varsigma \sigma(kr) dr \leq \frac{k\sigma'_M \varsigma^2}{2}, \forall \varsigma \in \mathbb{R}$.

4. $\int_0^\varsigma \sigma(kr) dr > 0, \forall \varsigma \neq 0$.

5. $\int_0^\varsigma \sigma(kr) dr \rightarrow \infty$ as $|\varsigma| \rightarrow \infty$.

6. If σ is strictly increasing, then

a. $\varsigma[\sigma(\varsigma + \eta) - \sigma(\eta)] > 0, \forall \varsigma \neq 0, \forall \eta \in \mathbb{R}$.

b. For any constant $a \in \mathbb{R}$, $\bar{\sigma}(\varsigma) = \sigma(\varsigma + a) - \sigma(a)$ is a strictly increasing generalized saturation function (SI-GSF) bounded by $\bar{M} = M + |\sigma(a)|$.

7. If σ is a L -GSF for (L, M) then $\varsigma[\sigma(\varsigma + \nu(\eta)) - \sigma(\nu(\eta))] > 0, \forall \varsigma \neq 0, \forall \eta \in \mathbb{R}$, for any continuous function $\nu: \mathbb{R} \mapsto \mathbb{R}$ such that $|\nu(\eta)| < L$.

According to the Euler-Lagrange methodology, the dynamic model of a n -degree-of-freedom robot interacting with its environment can be represented as

$$H(q)\ddot{q} + C(q, \dot{q})\dot{q} + F\dot{q} + g(q) = \tau - J^T(q)f_e, \quad (1)$$

where $q, \dot{q}, \ddot{q} \in \mathbb{R}^n$ are vectors of joint position, velocity and acceleration, respectively; $H(q), C(q, \dot{q}), F \in \mathbb{R}^{n \times n}$ are matrices of inertia, centripetal and Coriolis, and viscous friction, respectively; $J(q) \in \mathbb{R}^{m \times n}$ is the analytical Jacobian matrix; while, $g(q), \tau \in \mathbb{R}^n$ and $f_e \in \mathbb{R}^m$ are vectors of gravitational, control and environmental torques acting on the robot, respectively.

It is important to note that the dynamic model (1) has some properties that are relevant for the purposes of this work [41, 42].

Property 1. *For any robot manipulator, $H(q)$ and F are positive definite symmetric matrices, even F is diagonal.*

Property 2. *In the case of robot manipulators with only revolute joints, $g(q)$ is bounded on \mathbb{R}^n in such a way that $|g_i(q)| \leq B_{gi}, \forall q \in \mathbb{R}^n$ and $B_{gi} \geq 0, i = 1, \dots, n$.*

Property 3. *In the case of robot manipulators with only revolute joints, there are non-negative constants such that $\|J_i^T(y)\| \leq B_{Ji}, \forall y \in \mathbb{R}^n, i = 1, \dots, n$.*

It is well known that, due to the characteristics of the robot actuators and their corresponding electronic drivers, the control inputs of the robotic system are bounded and it gives rise to the following assumption.

Assumption 1. *Each component of vector τ is bounded by $T_i > 0$, i.e., $|\tau_i| \leq T_i, i = 1, \dots, n$, then assume that*

$$\tau_i = T_i \text{sat} \left(\frac{u_i}{T_i} \right), \quad (2)$$

where $\text{sat}(\cdot)$ is the standard saturation function, i.e. $\text{sat}(\zeta) = \text{sign}(\zeta) \min\{|\zeta|, 1\}$ and u_i is the i -th control signal. In addition, assume that $T_i > B_{gi}, \forall i \in \{1, \dots, n\}$.

Using the direct kinematic mapping $x = \mathcal{K}(q) \in \mathbb{R}^m$, the dynamic model (1) can be rewritten in task space as

$$H_x \ddot{x} + C_x \dot{x} + F_x \dot{x} + g_x = f_x - f_e \quad (3)$$

where $\dot{x} = J(q)\dot{q} \in \mathbb{R}^m$ is the task-space velocity, $\ddot{x} = \dot{J}(q, \dot{q})\dot{q} + J(q)\ddot{q} \in \mathbb{R}^m$ is the task-space acceleration, f_x is the vector of control forces such that $\tau = J^T(q)f_x$, $H_x = [J^{-1}(q)]^T H(q) J^{-1}(q)$, $C_x = \{[J^{-1}(q)]^T C(q, \dot{q}) - H_x \dot{J}(q, \dot{q})\} J^{-1}(q)$, $F_x = [J^{-1}(q)]^T F J^{-1}(q)$ and $g_x = [J^{-1}(q)]^T g(q)$. Note that the task-space dynamic

model (3) is valid when the robot is away from singular configurations and the right pseudo-inverse of $J(q)$ should be considered when the robot is redundant, i.e., $n > m$ [43].

The robot-environment interaction forces can be modeled in different ways, in our case we are considering the generalized model of a spring system.

Assumption 2. *The vector f_e can be modeled as*

$$f_e = K_e [x - x_e], \quad (4)$$

where $K_e \in \mathbb{R}^{m \times m}$ is a positive-definite diagonal stiffness matrix and $x_e \in \mathbb{R}^m$ is the rest position.

The permissible deformation of the environment before a fracture is bounded, therefore it is possible to assume that the robot-environment interaction forces can be represented by a bounded version of the generalized spring system.

Assumption 3. *A bounded version of model (4) can be represented by*

$$f_e = s_e(K_e[x - x_e]), \quad (5)$$

where $s_e(y) = (\sigma_{e1}(y_1), \dots, \sigma_{em}(y_m))^T$ with $\sigma_{ej}(\cdot)$ being strictly increasing LGSFs bounded by M_{ej} .

Also the dynamic model (3) has some relevant properties of interest for the further stability analysis [10–12]:

Property 4. *There exist constants $\mu_M \geq \mu_m > 0$ such that $H_x \in \mathbb{R}^{m \times m}$ satisfies $\mu_m I_m \leq H_x \leq \mu_M I_m$.*

Property 5. *There exists a constant $k_c \geq 0$ such that $C_x \in \mathbb{R}^{m \times m}$ satisfies $\|C_x \dot{x}\| \leq k_c \|\dot{x}\|^2, \forall \dot{x} \in \mathbb{R}^m$.*

Property 6. *There exist constants $f_M \geq f_m > 0$ such that $F_x \in \mathbb{R}^{m \times m}$ satisfies $f_m I_m \leq F_x \leq f_M I_m$.*

Property 7. *The matrices C_x and $\dot{H}_x \triangleq dH_x/dt$ satisfy $\dot{x}^T [\dot{H}_x - 2C_x] \dot{x} = 0, \forall \dot{x} \in \mathbb{R}^m$, and actually $\dot{H}_x = C_x + C_x^T$ (see proof in A).*

Recalling that the robot inputs are bounded, it is important to assume that this is also the case in task space.

Assumption 4. *According to Assumption 1 and Property 3, because $\tau = J^T(q) f_x$ each component of f_x can be bounded by a constant $\mathcal{F}_j > 0$, i.e., $|f_{xj}| \leq \mathcal{F}_j, j = 1, \dots, m$. Thus, assume that*

$$f_{xj} = \mathcal{F}_j \text{sat} \left(\frac{u_{xj}}{\mathcal{F}_j} \right) \quad (6)$$

and then $u = J^T(q) u_x$.

3. Nonlinear force/position controller without velocity measurement

To avoid the use of velocity sensors while regulating robot-environment interaction, the following force/position control structure is proposed

$$u_x = -s_F(K_F \bar{f}) - s_P(K_P \bar{x}) - s_D(K_D \vartheta) + g_x + f_e \quad (7)$$

where the force and position errors are given by $\bar{f} = f_e - f_d$ and $\bar{x} = x - x_d$ with $f_d, x_d \in \mathbb{R}^m$ being constant desired force and position vectors, respectively; $K_F = \text{diag}[k_{F1}, \dots, k_{Fm}]$, $K_P = \text{diag}[k_{P1}, \dots, k_{Pm}]$ and $K_D = \text{diag}[k_{D1}, \dots, k_{Dm}]$ are positive definite matrices of gain parameters; $s_F(y) = (\sigma_{F1}(y_1), \dots, \sigma_{Fm}(y_m))^T$ and $s_P(y) = (\sigma_{P1}(y_1), \dots, \sigma_{Pm}(y_m))^T$ with $\sigma_{Fj}(\cdot)$ and $\sigma_{Pj}(\cdot)$ being SI-GSFs bounded by M_{Fj} and M_{Pj} , respectively; $s_D(y) = (\sigma_{D1}(y_1), \dots, \sigma_{Dm}(y_m))^T$ with $\sigma_{Dj}(\cdot)$ being GSFs bounded by M_{Dj} and that satisfies

$$\|s_D(K_D \vartheta)\|^2 \leq \kappa \vartheta^T s_D(K_D \vartheta) \leq \kappa^2 \|\vartheta\|^2 \quad (8)$$

for some constant $\kappa > 0$ and $\forall \vartheta \in \mathbb{R}^m$ that represents the estimated velocity vector obtained from the following auxiliary dynamics

$$\dot{\vartheta}_c = -A[\vartheta_c + B\bar{x}], \quad (9)$$

$$\vartheta = \vartheta_c + B\bar{x}, \quad (10)$$

where $A, B \in \mathbb{R}^{m \times m}$ are positive definite diagonal matrices, i.e., $A = \text{diag}[a_1, \dots, a_m]$ and $B = \text{diag}[b_1, \dots, b_m]$ with $a_j > 0$, $b_j > 0$, $\forall j = 1, \dots, m$.

3.1. Closed-loop analysis

The closed-loop robot-environment interaction dynamics is obtained by combining the robot and environment models (3), (4) and the force/position controller (7), (9)-(10), such that

$$\dot{\bar{f}} = K_e \dot{\bar{x}}, \quad (11)$$

$$\dot{\bar{x}} = \dot{x}, \quad (12)$$

$$\dot{\vartheta} = -A\vartheta + B\dot{\bar{x}}, \quad (13)$$

$$H_x \ddot{x} = -s_F(K_F \bar{f}) - s_P(K_P \bar{x}) - s_D(K_D \vartheta) - C_x \dot{x} - F_x \dot{x}. \quad (14)$$

To analyze the existence of equilibrium point in the closed-loop system (11)-(14), under stationary conditions $\dot{\bar{f}} = \dot{\bar{x}} = \dot{\vartheta} = \ddot{x} = \dot{x} = 0_m$, we have that

$$-A\vartheta = 0_m, \quad (15)$$

$$-s_F(K_F \bar{f}) - s_P(K_P \bar{x}) - s_D(K_D \vartheta) = 0_m. \quad (16)$$

Then, $(\bar{f}_E, \bar{x}_E, \vartheta_E, \dot{x}_E)^T = (\bar{f}^*, \bar{x}^*, 0_m, 0_m)^T$ is the equilibrium vector such that

$$s_F (K_F \bar{f}^*) = -s_P (K_P \bar{x}^*), \quad (17)$$

where $\bar{f}_j^* = \sigma_{Fj}^{-1}(-\sigma_{Pj}(k_{Pj}\bar{x}_j^*))/k_{Fj}$, $\forall j = 1, \dots, m$.

3.2. Stability analysis

In order to analyze the stability of the closed-loop equilibrium vector, we use Lyapunov's direct method (see Theorem 4.1, [40, Section 4.1]) and the invariance principle (see Theorem 4.4, [40, Section 4.2]), and the corresponding procedure is described below.

Proposition 1. *Consider the dynamic closed-loop system (11)-(14) and Assumptions 1 and 4. Thus, for any positive definite diagonal matrices K_F , K_P and K_D , and any ϵ satisfying the following condition*

$$\epsilon < \epsilon_M \triangleq \min \{\epsilon_1, \epsilon_2, \epsilon_3, \epsilon_4\} \quad (18)$$

where

$$\epsilon_1 \triangleq \sqrt{\frac{\mu_m}{\mu_M^2(\beta_F + \beta_P)}}, \quad (19)$$

$$\epsilon_2 \triangleq \frac{\beta_d}{\kappa}, \quad (20)$$

$$\epsilon_3 \triangleq \frac{\beta_d f_m - \kappa}{\beta_d \beta_M}, \quad (21)$$

$$\epsilon_4 \triangleq \frac{f_m}{\beta_M + f_M^2} \quad (22)$$

with

$$\beta_F \triangleq \max_j \{\sigma'_{FjM} k_{Fj} k_{ej}\} \quad (23)$$

$$\beta_P \triangleq \max_j \{\sigma'_{PjM} k_{Pj}\} \quad (24)$$

$$\beta_d \triangleq \min_j \left\{ \frac{a_j}{b_j} \right\} > \frac{\kappa}{f_m} \quad (25)$$

$$\beta_M \triangleq k_c B_{FP} + \mu_M (\beta_F + \beta_P) \quad (26)$$

where $B_{FP} \triangleq \sqrt{\sum_{j=1}^m M_{Fj}^2} + \sqrt{\sum_{j=1}^m M_{Pj}^2}$, σ'_{FjM} and σ'_{PjM} are the positive bounds of $D^+ \sigma_{Fj}(\cdot)$ and $D^+ \sigma_{Pj}(\cdot)$, respectively (see item 2 of Definition 1), μ_m , μ_M , k_c , f_m and f_M as defined in Properties 4, 5 and 6, respectively, and κ as defined in (8); the asymptotic stability of the closed-loop equilibrium vector is guaranteed.

Remark 1. *It is important to note that conditions (18) and (25) are not necessary but only sufficient to ensure stability in closed loop, therefore there is a margin of tolerance without causing instability.*

Proof. In order to prove the stability of closed-loop equilibrium vector, we consider the following candidate function

$$\begin{aligned}
 V(\bar{x}, \bar{f}, \dot{x}, \vartheta) = & \frac{1}{2} \dot{x}^T H_x \dot{x} + \int_{0_m}^{\bar{f}} s_F^T(K_F r) K_e^{-1} dr + \epsilon \dot{x}^T H_x s_F(K_F \bar{f}) \\
 & + \frac{\kappa}{2} \vartheta^T B^{-1} \vartheta + \int_{0_m}^{\bar{x}} s_P^T(K_P r) dr + \epsilon \dot{x}^T H_x s_P(K_P \bar{x}). \quad (27)
 \end{aligned}$$

To demonstrate that this candidate function is positive definite, it can be rewritten as follows

$$\begin{aligned}
 V(\bar{x}, \bar{f}, \dot{x}, \vartheta) = & \frac{1}{2} \dot{x}^T H_x \dot{x} + \alpha \left[\int_{0_m}^{\bar{f}} s_F^T(K_F r) K_e^{-1} dr + \int_{0_m}^{\bar{x}} s_P^T(K_P r) dr \right] \\
 & + \epsilon \dot{x}^T H_x s_F(K_F \bar{f}) + \epsilon \dot{x}^T H_x s_P(K_P \bar{x}) + \frac{\kappa}{2} \vartheta^T B^{-1} \vartheta \\
 & + (1 - \alpha) \left[\int_{0_m}^{\bar{f}} s_F^T(K_F r) K_e^{-1} dr + \int_{0_m}^{\bar{x}} s_P^T(K_P r) dr \right] \quad (28)
 \end{aligned}$$

where $0 < \alpha < 1$ and by bounding some terms we get

$$\begin{aligned}
 V(\bar{x}, \bar{f}, \dot{x}, \vartheta) \geq & \frac{\mu_m}{2} \|\dot{x}\|^2 + \frac{\alpha}{2\beta_F} \|s_F(K_F \bar{f})\|^2 + \frac{\alpha}{2\beta_P} \|s_P(K_P \bar{x})\|^2 \\
 & - \epsilon \mu_M \|s_F(K_F \bar{f})\| \|\dot{x}\| - \epsilon \mu_M \|s_P(K_P \bar{x})\| \|\dot{x}\| \\
 & + (1 - \alpha) \left[\int_{0_m}^{\bar{f}} s_F^T(K_F r) K_e^{-1} dr + \int_{0_m}^{\bar{x}} s_P^T(K_P r) dr \right] \\
 & + \frac{\kappa}{2} \vartheta^T B^{-1} \vartheta \quad (29)
 \end{aligned}$$

using Property 4 and item 3 of Definition 1, then

$$V(\bar{x}, \bar{f}, \dot{x}, \vartheta) \geq (1 - \alpha) \left[\int_{0_m}^{\bar{f}} s_F^T(K_F r) K_e^{-1} dr + \int_{0_m}^{\bar{x}} s_P^T(K_P r) dr \right] + W_1(\bar{f}, \bar{x}, \dot{x}) + \frac{\kappa}{2} \vartheta^T B^{-1} \vartheta \quad (30)$$

where

$$W_1(\bar{f}, \bar{x}, \dot{x}) = \frac{1}{2} w_1^T \begin{bmatrix} \frac{\alpha}{\beta_F} & -\epsilon \mu_M & 0 \\ -\epsilon \mu_M & \mu_m & -\epsilon \mu_M \\ 0 & -\epsilon \mu_M & \frac{\alpha}{\beta_P} \end{bmatrix} w_1 \quad (31)$$

with $w_1 = (\|s_F(K_F \bar{f})\|, \|\dot{x}\|, \|s_P(K_P \bar{x})\|)^T$. Therefore, by selecting

$$\frac{\epsilon^2}{\epsilon_1^2} < \alpha < 1 \quad (32)$$

$W_1(\bar{f}, \bar{x}, \dot{x})$ is positive definite when the inequality (18) is fulfilled (see B), and $W_1(0_m, 0_m, \dot{x}) \rightarrow \infty$ as $\|\dot{x}\| \rightarrow \infty$. Therefore, in accordance with inequality (32) and the items 4 and 5 of Definition 1, we can concluded that $V(\bar{x}, \bar{f}, \dot{x}, \vartheta)$ is a positive definite and radially unbounded function.

The next step is to obtain the time derivative of the scalar function (27) along the trajectories of the closed-loop system (11)-(14), which is given by

$$\begin{aligned} \dot{V}(\bar{x}, \bar{f}, \dot{x}, \vartheta) &= \frac{1}{2} \dot{x}^T \dot{H}_x \dot{x} + \dot{x}^T H_x \ddot{x} + s_F^T(K_F \bar{f}) K_e^{-1} \dot{\bar{f}} + \epsilon s_F^T(K_F \bar{f}) H_x \ddot{x} \\ &\quad + \epsilon \dot{x}^T \dot{H}_x s_F(K_F \bar{f}) + \epsilon \dot{x}^T H_x s'_F(K_F \bar{f}) K_F \dot{\bar{f}} + \kappa \vartheta^T B^{-1} \dot{\vartheta} \\ &\quad + s_P^T(K_P \bar{f}) \dot{\bar{x}} + \epsilon s_P^T(K_P \bar{x}) H_x \ddot{x} + \epsilon \dot{x}^T \dot{H}_x s_P(K_P \bar{x}) \\ &\quad + \epsilon \dot{x}^T H_x s'_P(K_P \bar{x}) K_P \dot{\bar{x}} \\ &= \frac{1}{2} \dot{x}^T \dot{H}_x \dot{x} + \dot{x}^T [-s_F(K_F \bar{f}) - s_P(K_P \bar{x}) - s_D(K_D \vartheta) \\ &\quad - C_x \dot{x} - F_x \dot{x}] + s_F^T(K_F \bar{f}) \dot{x} + \epsilon s_F^T(K_F \bar{f}) [-s_F(K_F \bar{f}) \\ &\quad - s_P(K_P \bar{x}) - s_D(K_D \vartheta) - C_x \dot{x} - F_x \dot{x}] + \epsilon \dot{x}^T \dot{H}_x s_F(K_F \bar{f}) \\ &\quad + \epsilon \dot{x}^T H_x s'_F(K_F \bar{f}) K_F K_e \dot{x} + \kappa \vartheta^T B^{-1} [-A \vartheta + B \dot{x}] \\ &\quad + s_P^T(K_P \bar{f}) \dot{x} + \epsilon s_P^T(K_P \bar{x}) [-s_F(K_F \bar{f}) - s_P(K_P \bar{x}) \\ &\quad - s_D(K_D \vartheta) - C_x \dot{x} - F_x \dot{x}] + \epsilon \dot{x}^T \dot{H}_x s_P(K_P \bar{x}) \\ &\quad + \epsilon \dot{x}^T H_x s'_P(K_P \bar{x}) K_P \dot{x} \\ &= \dot{x}^T [\kappa \vartheta - s_D(K_D \vartheta)] - \dot{x}^T F_x \dot{x} - \epsilon s_F^T(K_F \bar{f}) s_F(K_F \bar{f}) \end{aligned}$$

$$\begin{aligned}
& -2\epsilon s_F^T(K_F \bar{f}) s_P(K_P \bar{x}) - \epsilon s_D^T(K_D \vartheta) [s_F(K_F \bar{f}) \\
& + s_P(K_P \bar{x})] - \epsilon \dot{x}^T C_x [s_F(K_F \bar{f}) + s_P(K_P \bar{x})] \\
& - \epsilon \dot{x}^T F_x [s_F(K_F \bar{f}) + s_P(K_P \bar{x})] \\
& + \epsilon \dot{x}^T H_x s'_F(K_F \bar{f}) K_F K_e \dot{x} - \kappa \vartheta^T B^{-1} A \vartheta \\
& - \epsilon s_P^T(K_P \bar{x}) s_P(K_P \bar{x}) + \epsilon \dot{x}^T H_x s'_P(K_P \bar{x}) K_P \dot{x}
\end{aligned} \tag{33}$$

where Property 7 was used. Then, in accordance with Properties 4-6, the function (33) can be bounded as

$$\begin{aligned}
\dot{V}(\bar{x}, \bar{f}, \dot{x}, \vartheta) \leq & \|\dot{x}\| \|\kappa \vartheta - s_D(K_D \vartheta)\| - f_m \|\dot{x}\|^2 - \epsilon \|s_F(K_F \bar{f}) \\
& + s_P(K_P \bar{x})\|^2 + \epsilon \|s_D(K_D \vartheta)\| \|s_F(K_F \bar{f}) + s_P(K_P \bar{x})\| \\
& + \epsilon k_c B_{FP} \|\dot{x}\|^2 + \epsilon f_M \|\dot{x}\| \|s_F(K_F \bar{f}) + s_P(K_P \bar{x})\| \\
& + \epsilon \mu_M \beta_F \|\dot{x}\|^2 - \kappa \beta_d \|\vartheta\|^2 + \epsilon \mu_M \beta_P \|\dot{x}\|^2
\end{aligned} \tag{34}$$

Observe that, in accordance with (8), $\kappa \vartheta^T s_D(K_D \vartheta) \geq \|s_D(K_D \vartheta)\|^2$. Hence,

$$\begin{aligned}
\|\kappa \vartheta - s_D(K_D \vartheta)\|^2 & = [\kappa \vartheta - s_D(K_D \vartheta)]^T [\kappa \vartheta - s_D(K_D \vartheta)] \\
& = \kappa^2 \vartheta^T \vartheta - 2\kappa \vartheta^T s_D(K_D \vartheta) + s_D^T(K_D \vartheta) s_D(K_D \vartheta) \\
& = \kappa^2 \|\vartheta\|^2 - 2\kappa \vartheta^T s_D(K_D \vartheta) + \|s_D(K_D \vartheta)\|^2 \\
& \leq \kappa^2 \|\vartheta\|^2 - 2\|s_D(K_D \vartheta)\|^2 + \|s_D(K_D \vartheta)\|^2 \\
& \leq \kappa^2 \|\vartheta\|^2 - \|s_D(K_D \vartheta)\|^2 \\
& \leq \kappa^2 \|\vartheta\|^2
\end{aligned} \tag{35}$$

then $\kappa \|\vartheta\| \geq \|\kappa \vartheta - s_D(K_D \vartheta)\|$. Thus,

$$\begin{aligned}
\dot{V}(\bar{x}, \bar{f}, \dot{x}, \vartheta) \leq & -\frac{1}{2} w_2^T \begin{bmatrix} \epsilon & -\epsilon \kappa \\ -\epsilon \kappa & \kappa \beta_d \end{bmatrix} w_2 - \frac{1}{2} w_3^T \begin{bmatrix} \kappa \beta_d & -\kappa \\ -\kappa & f_m - \epsilon \beta_M \end{bmatrix} w_3 \\
& - \frac{1}{2} w_4^T \begin{bmatrix} \epsilon & -\epsilon f_M \\ -\epsilon f_M & f_m - \epsilon \beta_M \end{bmatrix} w_4
\end{aligned} \tag{36}$$

where $w_2 = (\|s_F(K_F \bar{f}) + s_P(K_P \bar{x})\|, \|\vartheta\|)^T$, $w_3 = (\|\vartheta\|, \|\dot{x}\|)^T$ and $w_4 = (\|s_F(K_F \bar{f}) + s_P(K_P \bar{x})\|, \|\dot{x}\|)^T$. Therefore, when fulfilled (18), $\dot{V}(\bar{x}, \bar{f}, \dot{x}, \vartheta) \leq 0$ and by using LaSalle's invariance principle [40] with the following set

$$\begin{aligned}
\Omega & = \{ \bar{f}, \bar{x}, \dot{x}, \vartheta \in \mathbb{R}^m : \dot{V}(\bar{x}, \bar{f}, \dot{x}, \vartheta) = 0 \} \\
& = \{ \vartheta = \dot{x} = 0_m, \bar{f}, \bar{x} \in \mathbb{R}^m \}
\end{aligned} \tag{37}$$

Then, $\vartheta = \dot{x} = 0_m \Rightarrow \dot{\vartheta} = \ddot{x} = 0_m$ and from the closed-loop dynamics (11)-(14), $-s_F(K_F \bar{f}) - s_P(K_P \bar{x}) = 0_m$. Therefore, the closed-loop equilibrium vector is asymptotically stable, which completes the proof. \square

4. Force/position controller with bounded actions

When considering the environment model (5), the force/position controller (7), (9)–(10) is able to generate bounded control actions that allow to respect the torque limit values of the robot actuators. To prove it, by considering that Assumption 3 is fulfilled, (7) is rewritten as $u_x = u_{FPD} + g_x$ where

$$u_{FPD} = -s_F(K_F \bar{f}) - s_P(K_P \bar{x}) - s_D(K_D \vartheta) + s_e(K_e [x - x_e]). \quad (38)$$

Then, in order to avoid the actuator saturation

$$|u_i| = |J_i^T(q)u_x| = |J_i^T(q)u_{FPD} + g_x| < T_i \quad (39)$$

and in accordance with Property 2, Inequality (39) can be rewritten as

$$|J_i^T(q)u_{FPD}| \leq \|J_i^T(q)\| \|u_{FPD}\| < T_i - B_{gi}. \quad (40)$$

Therefore, from Property 3, the following sufficient condition to avoid saturation can be established

$$\sqrt{\sum_{j=1}^m [M_{Fj} + M_{Pj} + M_{Dj} + M_{ej}]^2} < \min_i \left\{ \frac{T_i - B_{gi}}{B_{Ji}} \right\} \triangleq u_M. \quad (41)$$

Remark 2. Because condition (41) is only sufficient and not necessary to avoid saturation, values greater than u_M can be considered.

5. Numerical simulation

To assess the effectiveness of the proposed control scheme, we conducted a numerical simulation of an interaction task in MATLAB® R2023b, employing the model of a three-degree-of-freedom anthropomorphic robot manipulator. The model of the robotic platform, along with its nominal parameters, is detailed in [44]. The maximum torques for this robot are $T_1 = 50$ Nm, $T_2 = 150$ Nm, and $T_3 = 15$ Nm, respectively.

To compare the performance of the proposed controller utilizing the velocity estimator with another scheme employing the backward difference approximation of velocity, we incorporated position and velocity measurements containing additive white noise. These measurements took into account the position sensor information provided by the manufacturers of robot actuators [44]. Specifically, we considered an error of 1 incremental-encoder pulse corresponding to 6.136×10^{-6} rad in the angular position measurement. A sampling period of 2.5 ms was utilized for the scheme employing the dirty derivative to compute velocity.

5.1. Description of the interaction task and configuration of the controller

Within the robot's workspace, a flat and rigid surface has been positioned for interaction with its end-effector. This task is illustrated in Fig. 1, showcasing the reference frame (x_p, y_p, z_p) affixed to the environment (surface), commonly referred to as a user frame in industrial robotics. The origin of this frame is situated at $(0.5, 0.35, -0.49)$ m. The planar surface is inclined at 30 degrees relative to the horizontal, with a stiffness value normal to the plane set at 2000 N/m, corresponding to $K_e = \text{diag}\{0, 1000, 1732.05\}$ N/m. Note that the position of the robot's end effector relative to the user frame is

$$\begin{bmatrix} x_{pe1} \\ x_{pe2} \\ x_{pe3} \\ 1 \end{bmatrix} = H_e^{-1} \begin{bmatrix} x_1 \\ x_2 \\ x_3 \\ 1 \end{bmatrix}, \quad (42)$$

where H_e is the following homogeneous transformation matrix

$$H_e = \begin{bmatrix} 0 & -1 & 0 & 0.5 \\ 0.866 & 0 & -0.5 & 0.35 \\ 0.5 & 0 & 0.866 & -0.49 \\ 0 & 0 & 0 & 1 \end{bmatrix}. \quad (43)$$

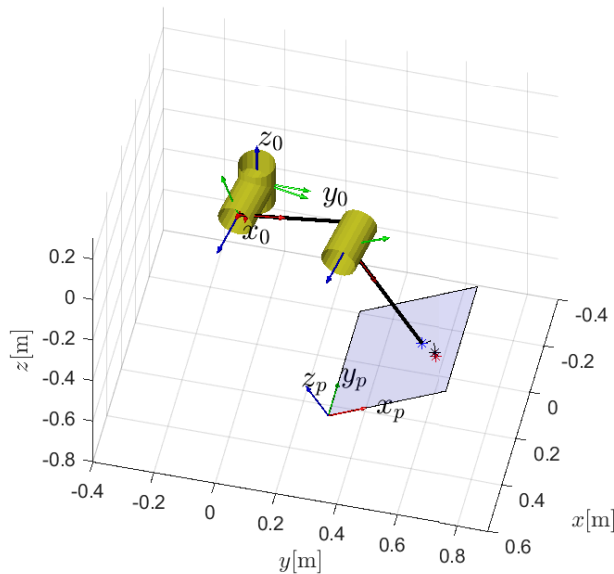


Figure 1: Graphical representation of the interaction task

The initial position of the robot was set at $q(0) = [-10, 110, -75]^T$ degrees, corresponding to the location of its end-effector at $x(0) = [0.364, 0.627, -0.215]^T$ m. The desired end-effector position is $x_d = [0.307, 0.658, -0.335]$ m. However, the flat surface serves as an obstacle, causing a robot-environment interaction. During this interaction, the robot needs to apply a normal force of 10 N, which is equivalent to $f_d = [0, -5, 8.66]^T$ N. It is important to note that the initial position of the robot is away from singularities. Figure 2 depicts the graphical representation of these singularities and demonstrates how the robot's path avoids them. The singularities correspond to points on the surface within the horizontal plane, *i.e.*, $\det[J(q)] \equiv 0$.

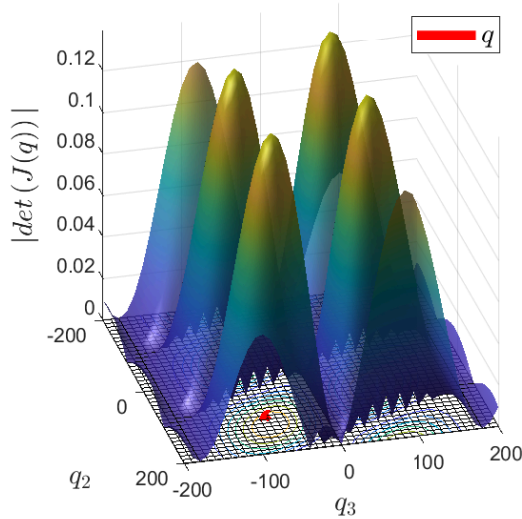


Figure 2: Graphical representation of singularities and the robot's trajectory for the interaction task. The axes for q_2 and q_3 are shown in degrees

On the other hand, the proposed controller (7) was implemented using the following generalized saturation functions

$$\sigma_h(\varsigma; M) = M \text{sat}(\varsigma/M), \quad (44)$$

$$\sigma_s(\varsigma; L, M) = \begin{cases} \varsigma, & \forall |\varsigma| \leq L, \\ \rho_s(\varsigma), & \forall |\varsigma| > L, \end{cases} \quad (45)$$

where

$$\rho_s(\varsigma) = \text{sign}(\varsigma)L + (M - L) \tanh\left(\frac{\varsigma - \text{sign}(\varsigma)L}{M - L}\right). \quad (46)$$

Then, the proportional actions of position, force, and velocity estimation were implemented with

$$\sigma_{Pj}(\zeta) = \sigma_s(\zeta; L_{Pj}, M_{Pj}), \quad (47)$$

$$\sigma_{Fj}(\zeta) = \sigma_s(\zeta; L_{Fj}, M_{Fj}), \quad (48)$$

$$\sigma_{Dj}(\zeta) = \sigma_h(\zeta; M_{Dj}), \quad (49)$$

$j = 1, \dots, 3$. Therefore, $\sigma'_{PjM} = \sigma'_{FjM} = \sigma'_{DjM} = 1$ and $\kappa = \max_j \{k_{Dj}\}$. The selected controller parameters are presented in Table 1. These values were employed for both the controller utilizing the velocity estimator and the one employing the backward difference approach.

Table 1: Parameter tuning for the controller utilized in numerical simulation tests

Parameter	Value
M_P	$[15, 10.2, 25]^T$
M_F	$[5, 8, 20]^T$
M_D	$[3, 5, 30]^T$
M_E	$[5, 10, 15]^T$
L_P	$0.9 \cdot M_P$
L_F	$0.9 \cdot M_F$
K_P	diag {650, 700, 40}
K_F	diag {3500, 800, 1560}
K_D	diag {100, 100, 100}
A	diag {160, 160, 160}
B	diag {160, 160, 160}

5.2. Results

The numerical simulation results are depicted in Figs. 3–6, where the subscript n refers to the controller utilizing the backward difference approximation for velocity estimation. In Fig. 3, the position errors ($\bar{x}_1, \bar{x}_2, \bar{x}_3$) corresponding to the components (x, y, z) of the world reference frame, respectively, are illustrated. It is notable that all components endeavor to approach zero; however, the contact of the end-effector with the surface impedes this achievement. Nonetheless, this contact is effectively regulated to prevent any damage, as evident from Fig. 4, where the force error components tend toward zero. It is crucial to highlight that the noise present in joint position measurements primarily impacts the estimation of Cartesian velocity when utilizing numerical differentiation. In contrast, the estimation using the subsystem (9)–(10) remains immune, as illustrated in Fig. 5.

Furthermore, this noise exerts influence on the transient response, delaying the moment of contact in the proposed scheme. Nevertheless, the control objective is still achieved. On the other hand, upon observing Fig. 6 which illustrates control torques, it can be confirmed that the proposed controller ensures the control torques remain bounded at all times.

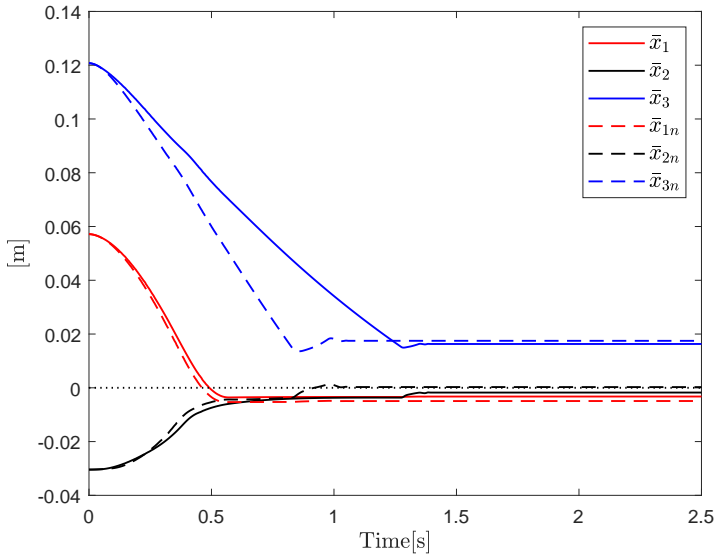


Figure 3: Components of position error obtained during numerical simulation tests

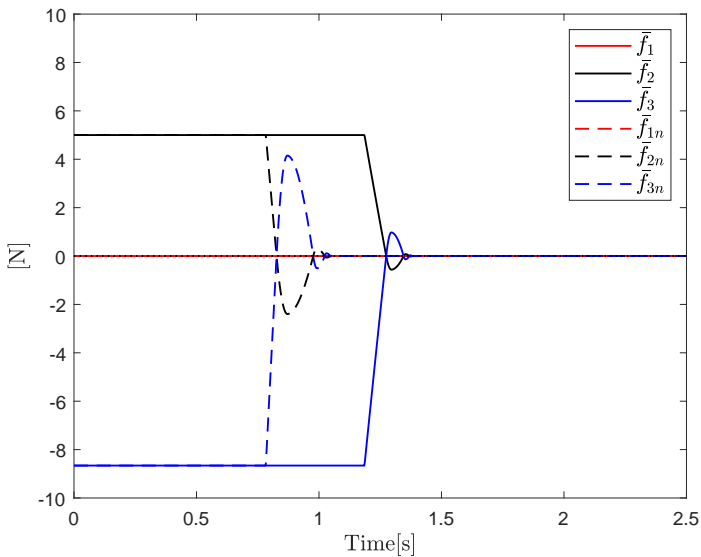


Figure 4: Components of force error obtained during numerical simulation tests

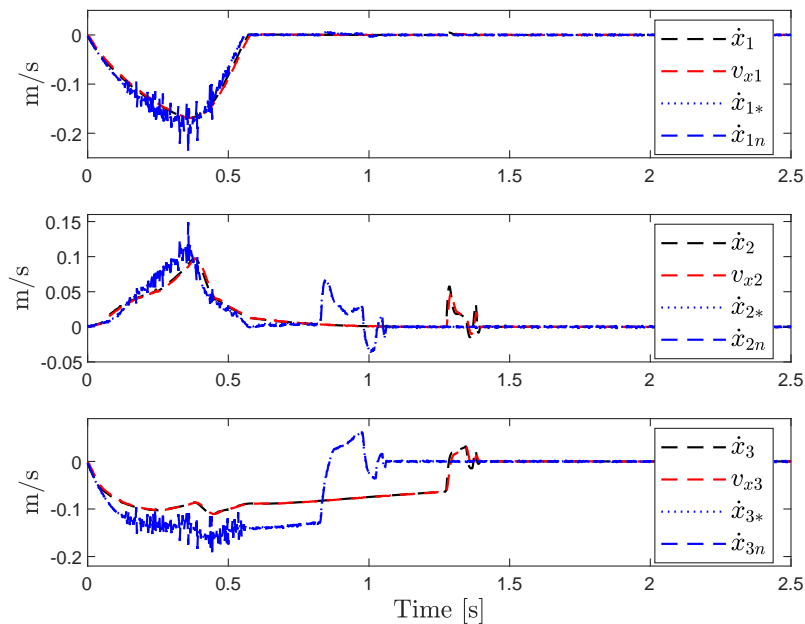


Figure 5: Velocity components obtained through position filtering and the dirty derivative method, respectively, during numerical simulation tests

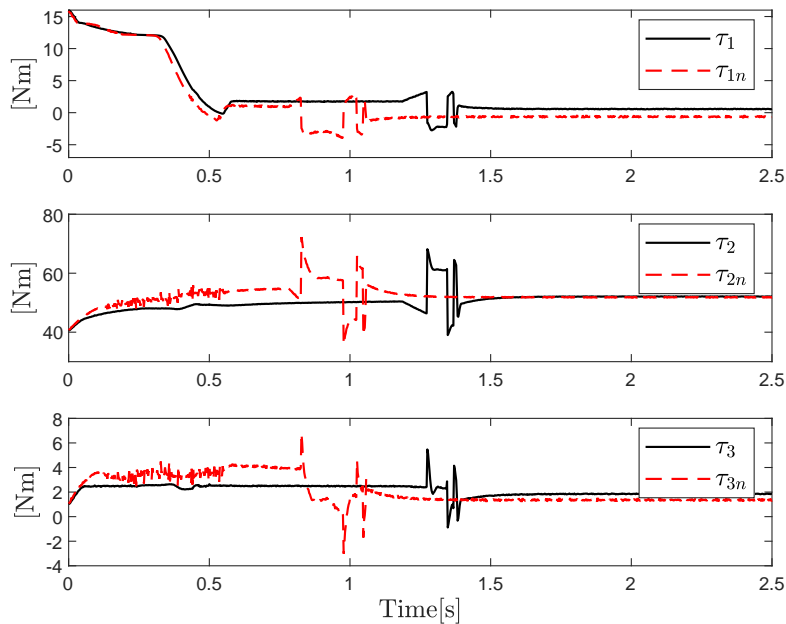


Figure 6: Components of control torque obtained during numerical simulation tests

To conduct a quantitative evaluation of the performance of both the proposed controller and the version utilizing numerical differentiation (dirty derivative), the following indices were taken into account:

1. \mathcal{L}_2 -norm, defined as

$$\|e\|_{\mathcal{L}_2} = \sqrt{\frac{1}{t-t_0} \int_{t_0}^t e^T(z)e(z) dz},$$

where $e \in \mathbb{R}^m$ represents the position or force error.

2. \mathcal{L}_∞ -norm, defined as

$$\|\mathcal{E}\|_{\mathcal{L}_\infty} = \max_t \{|\mathcal{E}(t)|\},$$

where $\mathcal{E}(t)$ represents the energy supplied to the kinematic chain (robot) at time t , defined as

$$\mathcal{E}(t) = \int_0^t \dot{q}^T(\sigma)\tau(\sigma) d\sigma.$$

Table 2 presents the performance indices obtained for each controller. The norms of position error and supplied energy were calculated throughout the entire simulation, while the norm of force error was computed only during the contact period. This commenced at approximately 1.185 s and 0.775 s for the schemes with velocity estimator and numerical differentiation, respectively. The numerical results lead us to conclude that the scheme utilizing numerical differentiation demonstrates slightly superior performance in terms of the position error index, attributed to its shorter transient period to reach contact compared to the scheme employing the velocity estimator subsystem (9)-(10). Nonetheless, the force error and supplied energy indices indicate that the proposed scheme expends less energy and exhibits less aggressiveness upon impact, ensuring greater safety for both the robot and its environment.

Table 2: Performance indices for the force/position controller utilizing the velocity estimator and the numerical differentiation (dirty derivative), respectively

Index	Velocity estimator	Numerical differentiation
\mathcal{L}_2 -norm of position error	0.057 m	0.051 m
\mathcal{L}_2 -norm of force error	1.488 N	1.507 N
\mathcal{L}_∞ -norm of supplied energy	5.594 J	6.087 J

6. Experimental results

We conducted a experimental test to validate the force/position control control scheme involving a two-dimensional interaction task as states the following sections.

6.1. Experimental robotic platform

The experimental platform showed in Fig. 7 consist on a two degree-of-freedom parallelogram SCARA-type robot manipulator. The kinematic chain is actuated by a pair of brushless motors and their corresponding drivers configured in torque mode, specifically, the servomotor SVM-220B and the servoamplifier SVA-2300. Both motors have a torque limit of 9.4 Nm and are equipped with built-in quadrature encoders that provide joint position measurements with a resolution of 10,000 pulses per revolution. The control algorithms are executed at 2 ms of sample time on an STM32F407 Discovery board. To get the interaction force for feedback, an ATI multi-axis F/T sensor is mounted on the robot's end-effector, specifically, the model Gamma, calibrated to measure a maximum force of 130 N and a maximum torque of 10 Nm about each axis.

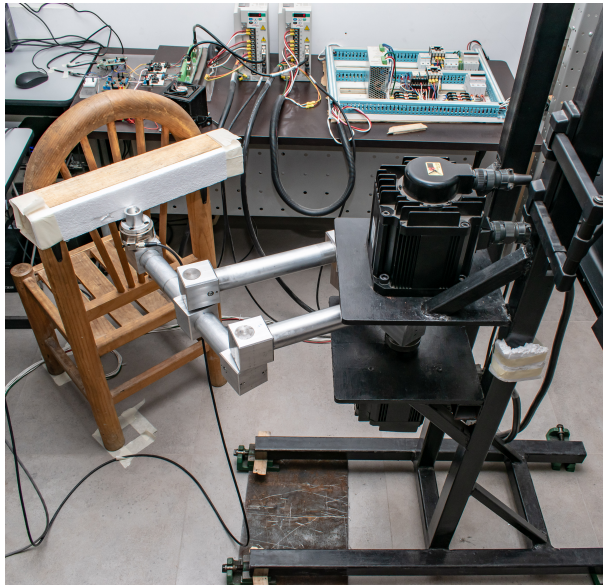


Figure 7: Experimental robotic platform

The kinematic diagram of the robot is illustrated in Fig. 8, with L_i representing the length of the i -th link. Specifically, $L_1 = L_4 = 0.35$ m, $L_2 = 0.45$ m and $L_3 = 0.1867$ m. The corresponding direct kinematic model $x(q)$ and the

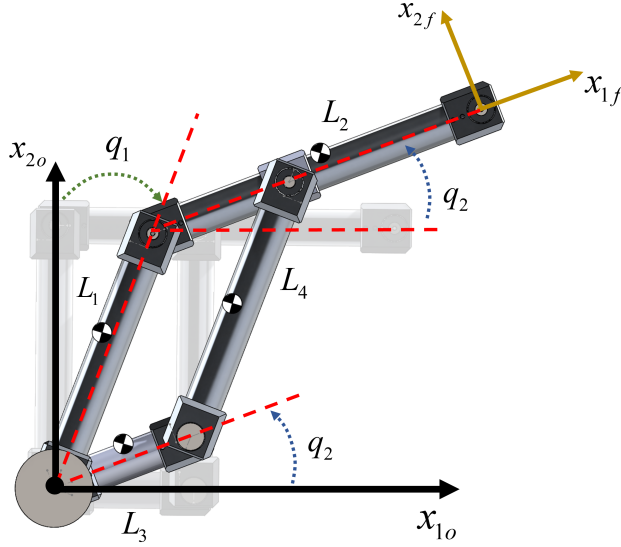


Figure 8: Kinematic diagram of the experimental robotic platform

Jacobian matrix $J(q)$ are given by

$$\begin{aligned} x(q) &= \begin{bmatrix} L_1 \sin q_1 + L_2 \cos q_2 \\ L_1 \cos q_1 + L_2 \sin q_2 \end{bmatrix}, \\ J(q) &= \begin{bmatrix} L_1 \cos q_1 & -L_2 \sin q_2 \\ -L_1 \sin q_1 & L_2 \cos q_2 \end{bmatrix}. \end{aligned} \quad (50)$$

The gravity field of earth is aligned to x_{3o} of the reference frame, consequently the potential energy of this robot is constant, hence the gravity vector $g(q)$ is null. The inertia, Coriolis and viscous friction matrices are given by

$$\begin{aligned} H(q) &= \begin{bmatrix} \varrho_1 & -\varrho_2 s_{1,2} - \varrho_3 c_{1,2} \\ -\varrho_2 s_{1,2} - \varrho_3 c_{1,2} & \varrho_4 \end{bmatrix} \\ C(q, \dot{q}) &= \begin{bmatrix} 0 & \dot{q}_2 (\varrho_3 s_{1,2} - \varrho_2 c_{1,2}) \\ \dot{q}_1 (\varrho_3 s_{1,2} - \varrho_2 c_{1,2}) & 0 \end{bmatrix} \\ F &= \begin{bmatrix} f_{v1} & 0 \\ 0 & f_{v2} \end{bmatrix} \end{aligned} \quad (51)$$

where $s_{1,2} = \sin(q_1 + q_2)$, $c_{1,2} = \cos(q_1 + q_2)$, and ϱ_j , $j = 1, \dots, 4$, are the robot parameters related to mass, centers of mass, and moments of inertia, while f_{v1} and f_{v2} are the viscous friction coefficients. The numerical values of these parameters are reported in Table 3.

Table 3: Parameters for the robot model

Parameter	Value	Units
ϱ_1	0.536032	Nm·s ² /rad
ϱ_2	0.295742	Nm·s ² /rad
ϱ_3	0.009131	Nm·s ² /rad
ϱ_4	0.336187	Nm·s ² /rad
f_{v1}	0.016366	Nm·s/rad
f_{v2}	0.019832	Nm·s/rad

6.2. Results

A robot-environment force interaction scenario was configured in order to validate the performance of the proposed scheme. The fixed environment consist on a solid, flat surfaced made on wooden wall covered with a styrofoam plate. The robot start its motion from a stationary position with joint configuration $q(0) = [45, -58]^T$ degrees, that is, the initial location of the robot end-effector is placed at $x(0) = [0.4860, -0.1341]^T$ meters. The tuning parameters for this experiment appear in Table 4. The reference force was configured as $f_d = [-6, 8]^T$ N, while the position target was $x_d = [0.6379, -0.3142]^T$ m. With this configuration for initial and target positions, the end-effector collides with the flat surface before achieving the position goal.

Table 4: Parameter tuning for the controller utilized in the experimental test

Parameter	Value
M_P	$[2.5, 2.5]^T$
M_F	$[2.5, 2.5]^T$
M_D	$[3.5, 3.5]^T$
M_E	$[10, 15]^T$
L_P	$0.9 \cdot M_P$
L_F	$0.9 \cdot M_F$
K_P	diag {8, 8}
K_F	diag {4, 5}
K_D	diag {70, 70}
A	diag {162.65, 162.65}
B	diag {162.65, 162.65}

The experimental findings are visually presented in Figs. 9–12. Figure 9 depicts the evolution of position error over time, showcasing its attempt to converge to the desired position. However, due to contact with a flat surface, achieving

the objective is hindered. Despite this, the position demonstrates stable behavior during the interaction.

Figure 10 displays the estimated Cartesian velocity, calculated through the subsystem described by equations (9) and (10). The figure reveals micro-oscillations, attributed to noise, yet the formulation of the estimator as a low-pass linear filter effectively mitigates this noise.

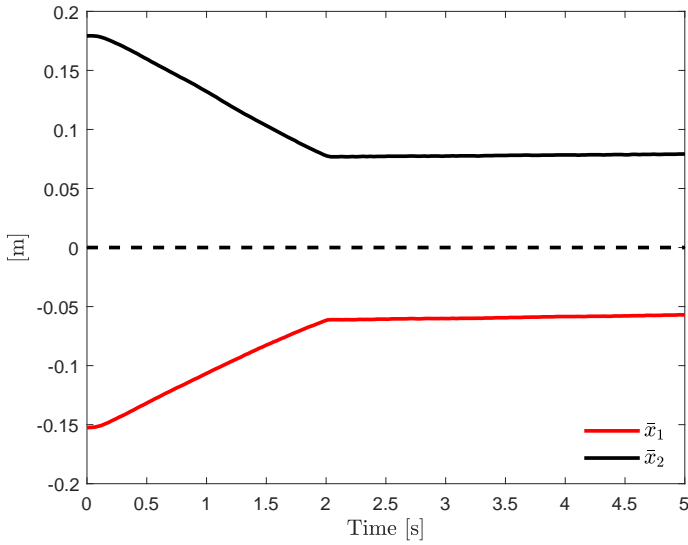


Figure 9: Components of position error obtained during the experimental test

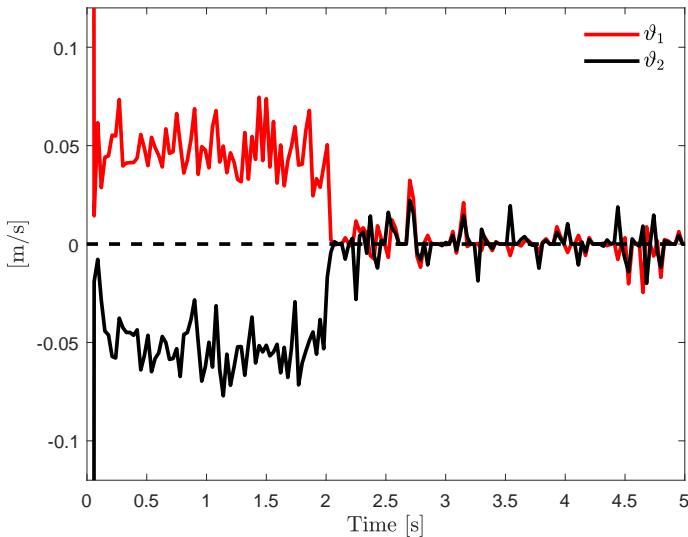


Figure 10: Components of estimated velocity obtained during the experimental test

The behavior of force error is elucidated in Fig. 11, where the presence of noise during free-space movement is observed. During contact, the amplification of noise is attributed to the proportional term in the force-position controller; nonetheless, the interaction remains stable.

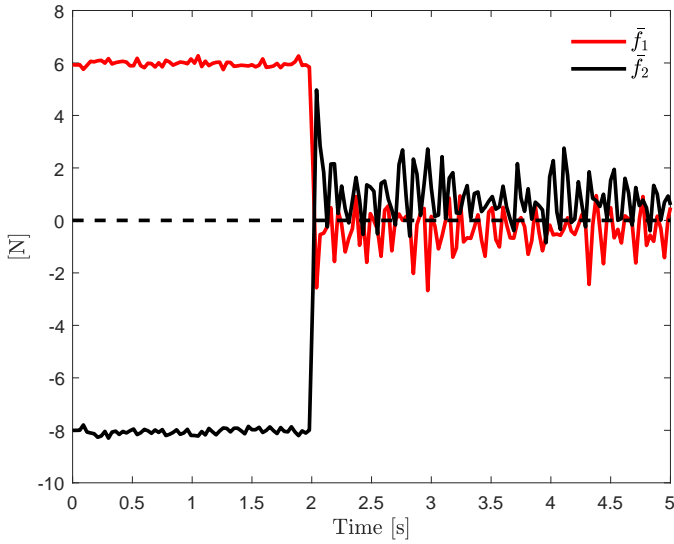


Figure 11: Components of force error obtained during the experimental test

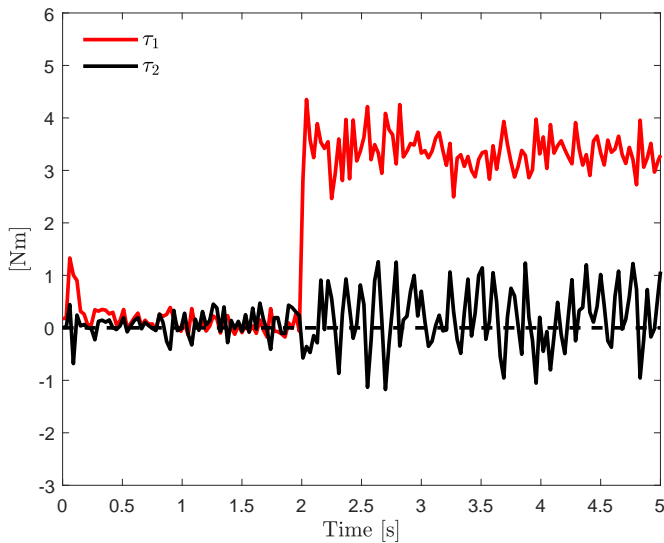


Figure 12: Components of control torque obtained during the experimental test

Lastly, Fig. 12 illustrates the control torques of the experiment, revealing that they stay within the limits of nominal values, ensuring a controlled and stable operation.

7. Conclusions

The work presented herein introduces an innovative nonlinear force/position controller tailored for robotic applications demanding precision in position control and interaction with the environment. This control scheme eliminates the need for speed measurement, which is advantageous in low-budget applications, with reduced maintenance and with the advantage of offering long-term reliable operation, without compromising the safety and efficiency of the robotic system.

The introduced control scheme integrates a filter for velocity estimation, addressing significant shortcomings observed in model-based schemes documented in the literature. This controller facilitates the generation of bounded control actions, and its stability is demonstrated in Lyapunov sense.

Validation of the proposed control scheme was conducted through numerical simulation tests of a three-degree-of-freedom anthropomorphic robot and experimentation on a two-degree-of-freedom SCARA-type robot manipulator. Both the simulation and experimental results validate the proposal in terms of stability during interaction with the environment, without exceeding the limits in the torques exerted by the robot actuators. Furthermore, according to the performance evaluation, the proposed scheme minimizes the effects of sensor noise, optimizes energy consumption, and enhances accuracy and safety in robot-environment interaction tasks.

A. Proof of skew symmetry of matrix $\dot{H}_x - 2C_x$

In order to prove that the matrix $\dot{H}_x - 2C_x$ is skew-symmetric, we first establish the validity of the expression $\dot{H}_x = C_x + C_x^T$. To achieve this, we begin by considering $\frac{d}{dt}H_x = \dot{H}_x$ as follows:

$$\begin{aligned}
 \dot{H}_x &= \frac{d}{dt} \{ [J^{-1}(q)]^T H(q) J^{-1}(q) \} \\
 &= \frac{d}{dt} \{ [J^{-1}(q)]^T \} H(q) J^{-1}(q) + [J^{-1}(q)]^T \frac{d}{dt} [H(q)] J^{-1}(q) \\
 &\quad + [J^{-1}(q)]^T H(q) \frac{d}{dt} [J^{-1}(q)]
 \end{aligned} \tag{53}$$

Now, to simplify the above expression, note that

$$\begin{aligned} \frac{d}{dt} [J(q)J^{-1}(q)] &= \frac{d}{dt} [I_m] \\ J(q)\frac{d}{dt} [J^{-1}(q)] + \frac{d}{dt} [J(q)] J^{-1}(q) &= 0_m \end{aligned} \quad (54)$$

then

$$\frac{d}{dt} [J^{-1}(q)] = -J^{-1}(q)\dot{J}(q, \dot{q})J^{-1}(q) \quad (55)$$

where $\dot{J}(q, \dot{q}) = \frac{d}{dt} [J(q)]$. Thus, with $[J(q)J^{-1}(q)]^T = I_m$, we obtain

$$\frac{d}{dt} [J^{-1}(q)]^T = -[J^{-1}(q)]^T \frac{d}{dt} [J^T(q)] [J^T(q)]^{-1} \quad (56)$$

Thus, by substituting equations (55) and (56) into (53), we can rewrite (53) as

$$\begin{aligned} \dot{H}_x &= -[J^{-1}(q)]^T \frac{d}{dt} [J^T(q)] H_x + [J^{-1}(q)]^T \dot{H}(q, \dot{q})J^{-1}(q) \\ &\quad - H_x \dot{J}(q, \dot{q})J^{-1}(q) \end{aligned} \quad (57)$$

where $\dot{H}(q, \dot{q}) = \frac{d}{dt} [H(q)]$ and $[J^T(q)]^{-1} = [J^{-1}(q)]^T$.

On the other hand,

$$\begin{aligned} C_x + C_x^T &= [J^{-1}(q)]^T C(q, \dot{q})J^{-1}(q) - H_x \dot{J}(q, \dot{q})J^{-1}(q) \\ &\quad + [J^{-1}(q)]^T C^T(q, \dot{q})J^{-1}(q) - [J^{-1}(q)]^T [\dot{J}(q, \dot{q})]^T H_x^T \\ &= [J^{-1}(q)]^T \dot{H}(q, \dot{q})J^{-1}(q) - H_x \dot{J}(q, \dot{q})J^{-1}(q) \\ &\quad - [J^{-1}(q)]^T \frac{d}{dt} [J^T(q)] H_x \end{aligned} \quad (58)$$

where, according to the well-known properties of the dynamic model [41, Chapter 4], $\dot{H}(q, \dot{q}) = C(q, \dot{q}) + C^T(q, \dot{q})$, H_x is a symmetric matrix, *i.e.*, $H_x = H_x^T$, as well as $\frac{d}{dt} [J^T(q)] = [\dot{J}(q, \dot{q})]^T$. Then, by comparing the equations (57) and (58), we can conclude that $\dot{H}_x = C_x + C_x^T$.

Next, we need to prove that $C_x^T - C_x = -[C_x^T - C_x]^T$. For this purpose consider that

$$\begin{aligned} C_x^T - C_x &= [J^{-1}(q)]^T C^T(q, \dot{q})J^{-1}(q) - [J^{-1}(q)]^T \frac{d}{dt} [J^T(q)] H_x^T \\ &\quad - [J^{-1}(q)]^T C(q, \dot{q})J^{-1}(q) + H_x \dot{J}(q, \dot{q})J^{-1}(q) \end{aligned} \quad (59)$$

On the other hand,

$$\begin{aligned}
 -[C_x^T - C_x]^T &= -\{[J^{-1}(q)]^T C^T(q, \dot{q}) J^{-1}(q)\}^T + \left\{[J^{-1}(q)]^T \frac{d}{dt} [J^T(q)] H_x^T\right\}^T \\
 &\quad + \{[J^{-1}(q)]^T C(q, \dot{q}) J^{-1}(q)\}^T - [H_x \dot{J}(q, \dot{q}) J^{-1}(q)]^T \\
 &= -[J^{-1}(q)]^T C(q, \dot{q}) J^{-1}(q) + H_x \dot{J}(q, \dot{q}) J^{-1}(q) \\
 &\quad + [J^{-1}(q)]^T C^T(q, \dot{q}) J^{-1}(q) - [J^{-1}(q)]^T \frac{d}{dt} [J^T(q)] H_x^T. \quad (60)
 \end{aligned}$$

Thus, by comparing the equations (59) and (60), we conclude that $C_x^T - C_x = -[C_x^T - C_x]^T$.

Finally, please note that

$$\begin{aligned}
 \dot{x}^T [\dot{H}_x - 2C_x] \dot{x} &= \dot{x}^T [C_x + C_x^T - 2C_x] \dot{x} \\
 &= \dot{x}^T [C_x^T - C_x] \dot{x} \\
 &= -\dot{x}^T [C_x^T - C_x]^T \dot{x} \\
 &= 0. \quad (61)
 \end{aligned}$$

Therefore, the matrix $\dot{H}_x - 2C_x$ is skew-symmetric, which completes the proof.

B. Proof of positive definiteness of $W_1(\bar{f}, \bar{x}, \dot{x})$

According to the definition of $W_1(\bar{f}, \bar{x}, \dot{x})$ in (31), consider the following symmetric matrix

$$A = \begin{bmatrix} \frac{\alpha}{\beta_F} & -\epsilon\mu_M & 0 \\ -\epsilon\mu_M & \mu_m & -\epsilon\mu_M \\ 0 & -\epsilon\mu_M & \frac{\alpha}{\beta_P} \end{bmatrix}. \quad (62)$$

Using the theorem of Sylvester [41], it is known that A is positive definite if and only if

$$\det[a_{11}] > 0, \quad \det \begin{bmatrix} a_{11} & a_{12} \\ a_{21} & a_{22} \end{bmatrix} > 0, \quad \det[A] > 0.$$

Therefore, because $\alpha > 0$ and $\beta_F > 0 \implies \det[\alpha/\beta_F] > 0$.

Then, to satisfy that

$$\det \begin{bmatrix} \frac{\alpha}{\beta_F} & -\epsilon\mu_M \\ -\epsilon\mu_M & \mu_m \end{bmatrix} = \frac{\alpha\mu_m}{\beta_F} - \mu_M^2 \epsilon^2 > 0 \quad (63)$$

it is necessary to select

$$\epsilon < \sqrt{\frac{\alpha\mu_m}{\mu_M^2\beta_F}} \triangleq \epsilon_0. \quad (64)$$

Finally,

$$\begin{aligned} \det [A] &= \frac{\alpha}{\beta_F} \begin{vmatrix} \mu_m & -\epsilon\mu_M \\ -\epsilon\mu_M & \frac{\alpha}{\beta_P} \end{vmatrix} + \epsilon\mu_M \begin{vmatrix} -\epsilon\mu_M & -\epsilon\mu_M \\ 0 & \frac{\alpha}{\beta_P} \end{vmatrix} \\ &= \frac{\alpha^2\mu_m}{\beta_F\beta_P} - \frac{\alpha\mu_M^2}{\beta_F}\epsilon^2 - \frac{\alpha\mu_M^2}{\beta_P}\epsilon^2 \\ &= \frac{\alpha^2\mu_m}{\beta_F\beta_P} - \left(\frac{1}{\beta_F} + \frac{1}{\beta_P}\right)\alpha\mu_M^2\epsilon^2. \end{aligned} \quad (65)$$

Therefore, to ensure that

$$\frac{\alpha\mu_m}{\beta_F\beta_P} > \left(\frac{1}{\beta_F} + \frac{1}{\beta_P}\right)\mu_M^2\epsilon^2 \quad (66)$$

it is required that

$$\epsilon < \sqrt{\frac{\alpha\mu_m}{\mu_M^2(\beta_F + \beta_P)}} \triangleq \epsilon_1 \quad (67)$$

and as $\epsilon_1 < \epsilon_0$, when fulfilled (67), it is concluded that $A > 0$. In addition, according to (66) and (67), note that

$$\alpha > \frac{(\beta_F + \beta_P)\mu_M^2\epsilon^2}{\mu_m}, \quad (68)$$

$$\frac{\epsilon^2}{\epsilon_1^2} = \frac{(\beta_F + \beta_P)\mu_M^2\epsilon^2}{\alpha\mu_m} < 1. \quad (69)$$

Then, it is always possible to select a positive constant $\alpha < 1$ that satisfies (32) and the quadratic function $W_1(\bar{f}, \bar{x}, \dot{x})$ is positive definite, which completes the proof.

References

- [1] J. CHO, D. CHOI and J.H. PARK: Sensorless variable admittance control for human-robot interaction of a dual-arm social robot. *IEEE Access*, **11** (2023), 69366–69377. DOI: [10.1109/ACCESS.2023.3292933](https://doi.org/10.1109/ACCESS.2023.3292933)
- [2] S.E. OVUR and Y. DEMIRIS: Naturalistic robot-to-human bimanual handover in complex environments through multi-sensor fusion. *IEEE Transactions on Automation Science and Engineering*, (2023). DOI: [10.1109/TASE.2023.3284668](https://doi.org/10.1109/TASE.2023.3284668)

- [3] Q. WU, H. LIU and Y. CHEN: Development of a hierarchical control strategy for a soft knee exoskeleton based on wearable multi-sensor system. *Proceedings of the Institution of Mechanical Engineers, Part I: Journal of Systems and Control Engineering*, **237**(9), (2023), 1587–1601. DOI: [10.1177/09596518231165345](https://doi.org/10.1177/09596518231165345)
- [4] M. JAVAID, A. HALEEM, R.P. SINGH and R. SUMAN: Substantial capabilities of robotics in enhancing industry 4.0 implementation. *Cognitive Robotics*, **1** (2021), 58–75. DOI: [10.1016/j.cogr.2021.06.001](https://doi.org/10.1016/j.cogr.2021.06.001)
- [5] A. BUERKLE, W. EATON, N. LOHSE, T. BAMBER and P. FERREIRA: EEG based arm movement intention recognition towards enhanced safety in symbiotic human-robot collaboration. *Robotics and Computer-Integrated Manufacturing*, **70** (2021), 102137. DOI: [10.1016/j.rcim.2021.102137](https://doi.org/10.1016/j.rcim.2021.102137)
- [6] S. WANG, J. ZHANG, P. WANG, J. LAW, R. CALINESCU and L. MIHAYLOVA: A deep learning-enhanced digital twin framework for improving safety and reliability in human–robot collaborative manufacturing. *Robotics and Computer-Integrated Manufacturing*, **85** (2024), 102608. DOI: [10.1016/j.rcim.2023.102608](https://doi.org/10.1016/j.rcim.2023.102608)
- [7] G. WANG, Z. WANG, B. HUANG, Y. GAN and F. MIN: Active compliance control based on EKF torque fusion for robot manipulators. *IEEE Robotics and Automation Letters*, **8**(5), (2023), 2668–2675. DOI: [10.1109/LRA.2023.3258697](https://doi.org/10.1109/LRA.2023.3258697)
- [8] Y. WU, H. FANG, T. XU and F. WAN: Adaptive fixed-time minimal learning force/position control of uncertain manipulators subject to input saturation. *International Journal of Adaptive Control and Signal Processing*, **37**(3), (2023), 790–810. DOI: [10.1002/acs.3549](https://doi.org/10.1002/acs.3549)
- [9] M. ISKANDAR, C. OTT, A. ALBU-SCHÄFFER, B. SICILIANO and A. DIETRICH: Hybrid force-impedance control for fast end-effector motions. *IEEE Robotics and Automation Letters*, **8**(7), (2023), 3931–3938. DOI: [10.1109/LRA.2023.3270036](https://doi.org/10.1109/LRA.2023.3270036)
- [10] C. CHÁVEZ-OLIVARES, F. REYES-CORTÉS and E. GONZÁLEZ-GALVÁN: On explicit force regulation with active velocity damping for robot manipulators. *Automatika*, **56**(4), (2015), 478–490. DOI: [10.1080/00051144.2015.11828661](https://doi.org/10.1080/00051144.2015.11828661)
- [11] L. ROJAS-GARCÍA, I. BONILLA-GUTIÉRREZ, M. MENDOZA-GUTIÉRREZ and C. CHÁVEZ-OLIVARES: Adaptive force/position control of robot manipulators with bounded inputs. *Journal of Mechanical Science and Technology*, **36**(3), (2022), 1497–1509. DOI: [10.1007/s12206-022-0236-1](https://doi.org/10.1007/s12206-022-0236-1)
- [12] L. ROJAS-GARCÍA, M. MENDOZA, I. BONILLA and C. CHÁVEZ-OLIVARES: Adaptive force control with active damping for robot manipulators with bounded inputs. *Computational and Applied Mathematics*, **41**(6), (2022), 266. DOI: [10.1007/s40314-022-01976-2](https://doi.org/10.1007/s40314-022-01976-2)
- [13] I. BONILLA, M. MENDOZA, D.U. CAMPOS-DELGADO and D.E. HERNÁNDEZ-ALFARO: Adaptive impedance control of robot manipulators with parametric uncertainty for constrained path-tracking. *International Journal of Applied Mathematics and Computer Science*, **28**(2), (2018), 363–374. DOI: [10.2478/amcs-2018-0027](https://doi.org/10.2478/amcs-2018-0027)
- [14] V.I. RAMÍREZ-VERA, M.O. MENDOZA-GUTIÉRREZ and I. BONILLA-GUTIÉRREZ: Impedance control with bounded actions for human–robot interaction. *Arabian Journal for Science and Engineering*, **47**(11), (2022), 14989–15000. DOI: [10.1007/s13369-022-06638-3](https://doi.org/10.1007/s13369-022-06638-3)

- [15] M. GUO, H. ZHANG, C. FENG, M. LIU and J. HUO: Manipulator residual estimation and its application in collision detection. *Industrial Robot: An International Journal*, **45**(3), (2018), 354–362. DOI: [10.1108/IR-01-2018-0019](https://doi.org/10.1108/IR-01-2018-0019)
- [16] P. CAO, Y. GAN and X. DAI: Finite-time disturbance observer for robotic manipulators. *Sensors*, **19**(8), (2019). DOI: [10.3390/s19081943](https://doi.org/10.3390/s19081943)
- [17] T. SUN and H. LIU: Adaptive force and velocity control based on intrinsic contact sensing during surface exploration of dynamic objects. *Autonomous Robots*, **44**(5), (2020), 773–790. DOI: [10.1007/s10514-019-09896-7](https://doi.org/10.1007/s10514-019-09896-7)
- [18] J. HU and R. XIONG: Contact force estimation for robot manipulator using semiparametric model and disturbance Kalman filter. *IEEE Transactions on Industrial Electronics*, **65**(4), (2018), 3365–3375. DOI: [10.1109/TIE.2017.2748056](https://doi.org/10.1109/TIE.2017.2748056)
- [19] G. PENG, C. YANG, W. HE and C.L.P. CHEN: Force sensorless admittance control with neural learning for robots with actuator saturation. *IEEE Transactions on Industrial Electronics*, **67**(4), (2020), 3138–3148. DOI: [10.1109/TIE.2019.2912781](https://doi.org/10.1109/TIE.2019.2912781)
- [20] M. HANAFUSA and J. ISHIKAWA: Mechanical impedance control of cooperative robot during object manipulation based on external force estimation using recurrent neural network. *Unmanned Systems*, **8**(3), (2020), 239–251. DOI: [10.1142/S230138502050017X](https://doi.org/10.1142/S230138502050017X)
- [21] S. YAO, Y. ZHUANG, Z. LI and R. SONG: Adaptive admittance control for an ankle exoskeleton using an EMG-driven musculoskeletal model. *Frontiers in Neurorobotics*, **12** (2018). DOI: [10.3389/fnbot.2018.00016](https://doi.org/10.3389/fnbot.2018.00016)
- [22] P. SONG, Y. YU and X. ZHANG: A tutorial survey and comparison of impedance control on robotic manipulation. *Robotica*, **37**(5), (2019), 801–836. DOI: [10.1017/S0263574718001339](https://doi.org/10.1017/S0263574718001339)
- [23] H. HU, X. WANG and L. CHEN: Impedance with finite-time control scheme for robot-environment interaction. *Mathematical Problems in Engineering*, **2020** (2020), 2796590. DOI: [10.1155/2020/2796590](https://doi.org/10.1155/2020/2796590)
- [24] M. LIN, H. WANG, J. NIU, Y. TIAN, X. WANG, G. LIU and L. SUN: Adaptive admittance control scheme with virtual reality interaction for robot-assisted lower limb strength training. *Machines*, **9**(11), (2021). DOI: [10.3390/machines9110301](https://doi.org/10.3390/machines9110301)
- [25] A. MARBAN, V. SRINIVASAN, W. SAMEK, J. FERNÁNDEZ and A. CASALS: A recurrent convolutional neural network approach for sensorless force estimation in robotic surgery. *Biomedical Signal Processing and Control*, **50** (2019), 134–150. DOI: [10.1016/j.bspc.2019.01.011](https://doi.org/10.1016/j.bspc.2019.01.011)
- [26] D.-K. KO, K.-W. LEE, D.H. LEE and S.-C. LIM: Vision-based interaction force estimation for robot grip motion without tactile/force sensor. *Expert Systems with Applications*, **211** (2023), 118441. DOI: [10.1016/j.eswa.2022.118441](https://doi.org/10.1016/j.eswa.2022.118441)
- [27] J. JIANG and S. LUO: Chapter 2: Robotic perception of object properties using tactile sensing. In: Q. Li, S. Luo, Z. Chen, C. Yang, J. Zhang (Eds.), *Tactile Sensing, Skill Learning, and Robotic Dexterous Manipulation*, Academic Press, 2022, pp. 23–44. DOI: [10.1016/B978-0-32-390445-2.00009-X](https://doi.org/10.1016/B978-0-32-390445-2.00009-X)
- [28] J. XU, J. PAN, T. CUI, S. ZHANG, Y. YANG and T.-L. REN: Recent progress of tactile and force sensors for human-machine interaction. *Sensors*, **23**(4), (2023). DOI: [10.3390/s23041868](https://doi.org/10.3390/s23041868)

- [29] Z. DENG, Y. JONETZKO, L. ZHANG and J. ZHANG: Grasping force control of multi-fingered robotic hands through tactile sensing for object stabilization. *Sensors*, **20**(4), (2020). DOI: [10.3390/s20041050](https://doi.org/10.3390/s20041050)
- [30] A. WAHRBURG, J. BÖS, K.D. LISTMANN, F. DAI, B. MATTHIAS and H. DING: Motor-current-based estimation of cartesian contact forces and torques for robotic manipulators and its application to force control. *IEEE Transactions on Automation Science and Engineering*, **15**(2), (2018), 879–886. DOI: [10.1109/TASE.2017.2691136](https://doi.org/10.1109/TASE.2017.2691136)
- [31] X. LIU, G. ZUO, J. ZHANG and J. WANG: Sensorless force estimation of end-effect upper limb rehabilitation robot system with friction compensation. *International Journal of Advanced Robotic Systems*, **16**(4), (2019), 1729881419856132. DOI: [10.1177/1729881419856132](https://doi.org/10.1177/1729881419856132)
- [32] S.-H. YEN, P.-C. TANG, Y.-C. LIN and C.-Y. LIN: Development of a virtual force sensor for a low-cost collaborative robot and applications to safety control. *Sensors*, **19**(11), (2019). DOI: [10.3390/s19112603](https://doi.org/10.3390/s19112603)
- [33] M.A. ARTEAGA and A. GUTIERREZ–GILES: On the robustness of force estimation methods for robot manipulators: An experimental study. *Journal of the Franklin Institute*, **360**(16), (2023), 11705–11735. DOI: [10.1016/j.jfranklin.2023.09.015](https://doi.org/10.1016/j.jfranklin.2023.09.015)
- [34] L. DING, H. XING, H. GAO, A. TORABI, W. LI and M. TAVAKOLI: VDC-based admittance control of multi-DOF manipulators considering joint flexibility via hierarchical control framework. *Control Engineering Practice*, **124** (2022), 105186. DOI: [10.1016/j.conengprac.2022.105186](https://doi.org/10.1016/j.conengprac.2022.105186)
- [35] L. ROVEDA and D. PIGA: Sensorless environment stiffness and interaction force estimation for impedance control tuning in robotized interaction tasks. *Autonomous Robots*, **45** (2021), 371–388. DOI: [10.1007/s10514-021-09970-z](https://doi.org/10.1007/s10514-021-09970-z)
- [36] S.B. LIU, A. GIUSTI and M. ALTHOFF: Velocity estimation of robot manipulators: An experimental comparison. *IEEE Open Journal of Control Systems*, **2** (2022) 1–11. DOI: [10.1109/OJCSYS.2022.3222753](https://doi.org/10.1109/OJCSYS.2022.3222753)
- [37] A. GUTIÉRREZ–GILES and M. ARTEAGA–PÉREZ: Output feedback hybrid force/motion control for robotic manipulators interacting with unknown rigid surfaces. *Robotica*, **38**(1), (2020), 136–158. DOI: [10.1017/S0263574719000523](https://doi.org/10.1017/S0263574719000523)
- [38] Z. ZHANG, M. LEIBOLD and D. WOLLHERR: Integral sliding-mode observer-based disturbance estimation for Euler–Lagrangian systems. *IEEE Transactions on Control Systems Technology*, **28**(6), (2020), 2377–2389. DOI: [10.1109/TCST.2019.2945904](https://doi.org/10.1109/TCST.2019.2945904)
- [39] H.H. KIM, M.C. LEE, J.H. KYUNG and H.M. DO: Evaluation of force estimation method based on sliding perturbation observer for dual-arm robot system. *International Journal of Control, Automation and Systems*, **19**(1), (2021), 1–10. DOI: [10.1007/s12555-019-0324-x](https://doi.org/10.1007/s12555-019-0324-x)
- [40] H. KHALIL: *Nonlinear Systems*. Pearson, India, 2014, 3rd Ed.
- [41] R. KELLY, V. SANTIBÁÑEZ and A. LORÍA: *Control of Robot Manipulators in Joint Space*. London, Springer, 2006.
- [42] M. RODRÍGUEZ-LIÑÁN, M. MENDOZA, I. BONILLA and C. CHÁVEZ-OLIVARES: Saturating stiffness control of robot manipulators with bounded inputs. *International Journal of Applied Mathematics and Computer Science*, **27**(1), (2017), 79–90. DOI: [10.1515/amcs-2017-0006](https://doi.org/10.1515/amcs-2017-0006)

- [43] C. CANUDAS, B. SICILIANO and G. BASTIN: *Theory of Robot Control*. London, Springer, 2012.
- [44] C. CHÁVEZ-OLIVARES, F. REYES-CORTÉS, E. GONZÁLEZ-GALVÁN, M. MENDOZA-GUTIÉRREZ and I. BONILLA-GUTIÉRREZ: Experimental evaluation of parameter identification schemes on an anthropomorphic direct drive robot. *International Journal of Advanced Robotic Systems*, **9**(5), (2012). DOI: [10.5772/52190](https://doi.org/10.5772/52190)